

Cavity-assisted boosting of self-hybridization between excitons and photonic bound states in the continuum in multilayers of transition metal dichalcogenides


Peng Xie,¹ Qi Ding,¹ Zhengchen Liang,^{1,2} Shiyu Shen,³ Ling Yue,¹ Hong Zhang,^{1,4} and Wei Wang^{1,*}

¹College of Physics, Sichuan University, Chengdu 610064, China

²Department of Physics, Tsinghua University, Beijing 100084, China

³Institute of Atomic and Molecular Physics, Sichuan University, Chengdu 610065, China

⁴Key Laboratory of High Energy Density Physics and Technology of Ministry of Education, Sichuan University, Chengdu 610065, China

 (Received 22 October 2022; revised 2 February 2023; accepted 3 February 2023; published 10 February 2023)

Strong coupling between excitons in transition metal dichalcogenides (TMDs) and quasibound states in the continuum (QBIC) has attracted much attention in recent years. However, the coupling strength is often limited due to the spatial mismatch at the location of the TMDs and the maximum field strength of the QBIC mode. Here, we report a cavity-assisted boosting of self-hybridization between excitons (X) and the QBIC mode at room temperature by embedding a two-dimensional (2D) metasurface composed of bulk WS₂ into a microcavity. We demonstrate that the self-hybridized BIC-X coupling strength in this 2D metasurface can be dramatically enhanced with the assistance of a Fabry-Pérot cavity. Full wave simulations demonstrate a giant Rabi splitting up to 240 meV, which is twice as high as the QBIC-X self-hybridization in the 2D metasurface system. A coupled oscillator model containing a 3×3 Hamiltonian matrix combined with a near-field analysis reveals the underlying mechanism of the greatly enlarged coupling strength: The cavity provides a strong out-of-plane field confinement and the QBIC mode concentrates in an in-plane electric field, which greatly facilitates the spatial overlap of excitons with the localized field. Importantly, we also demonstrate that the coupling strength of the hybrid system can be readily tuned by controlling the excitonic oscillator strength of the bulk TMD material. This provides a powerful approach for manipulating the self-hybridization process. We believe that the cavity-based configuration proposed in this paper can serve as a universal recipe for achieving strong light-matter interactions, thus paving the way for the design of tunable exciton-polariton photonic devices with high performance.

DOI: [10.1103/PhysRevB.107.075415](https://doi.org/10.1103/PhysRevB.107.075415)

I. INTRODUCTION

Strong coupling between transition metal dichalcogenides (TMDs) with other optical excitations has attracted much attention in the last decade, which provides us with an ideal platform to manipulate light-matter interactions at the nanoscale [1–6]. The new hybrid states formed by strong coupling, i.e., exciton polaritons with half-light and half-matter features, are of great importance for both fundamental physics including Bose-Einstein condensation [7] and superfluids [8], as well as many exciting applications such as low threshold polariton lasing [9] and quantum computing [10].

In the strong-coupling regime, the coupling strength g is usually determined as $g = \sqrt{N}\mu_e \cdot \mathbf{E} \propto \mu_e \sqrt{N/V}$, which is relevant to the inner product of the exciton transition dipole moment in TMDs and the local electric field [4,11]. To enhance the coupling strength, it is necessary to reduce the mode volume of the optical resonator. Recently, the strong coupling between TMDs and various plasmonic optical resonators such as single metallic nanoparticles, metallic hole arrays, and nanodisk lattices has been extensively studied [12–19]. These plasmonic resonators can confine light in the subwavelength

range, thus providing an ultrasmall mode volume with ultrastrong local field enhancement [20,21]. However, metallic resonators suffer from large intrinsic ohmic losses, complex preparation processes, and heat generation, which may hinder their applicability [22,23].

Mie resonances induced by dielectric nanoparticles with a high refractive index have been proposed as alternative platforms for the study of light-matter interactions [24–26]. Such dielectric nanocavities not only possess the property of reduced ohmic loss, but also have a complementary metal-oxide-semiconductor compatibility [27–29]. However, all-dielectric nanosystems typically exhibit a weaker electromagnetic field enhancement compared to plasmonic heterostructures, which limits the strong coupling in hybrid systems with a coupling strength reaching only on the order of tens of meV [30]. Therefore, it is highly desirable to develop strongly coupled hybrid systems that simultaneously possess a low intrinsic absorption loss and strong local field enhancement.

Recently, all-dielectric nanostructures supporting bound states in the continuum (BIC) have attracted much interest in achieving strong coupling with excitons (X) in TMDs [31,32]. The BIC resonance is generally associated with the simultaneous excitation of optical modes such as electric, magnetic, and higher-order electric quadrupoles [33]. The rich physics

*w.wang@scu.edu.cn

of BICs has been explored in the last decade by introducing in-plane symmetry breaking to induce finite but high- Q -factor quasi-BICs (QBIC), especially in boosting light-matter interactions [34–36]. In 2018, Koshelev *et al.* theoretically constructed a hybrid system composed of a WSe_2 monolayer placed on a one-dimensional (1D) Ta_2O_5 grating to realize strong X-BIC coupling [37]. Since then strong coupling between various types of QBIC modes excited by different 1D photonic crystals or two-dimensional (2D) metasurfaces and monolayer TMDs has been demonstrated theoretically or experimentally [31,38–40]. However, in the pursuit of large coupling strengths, it typically requires the layout of the monolayer TMDs at the maximum local field position of the QBIC mode, which leaves the full potential of the QBIC unexploited. The coupling strength is limited to a few tens of meV.

The coupling of bulk TMD excitons with the features of a high refractive index and strong excitonic absorption peaks to self-hybridized optical modes would potentially overcome this limitation, as it makes it possible to realize a full spatial overlap of excitons with the localized electric field. So far, excitons in bulk TMDs have been used to couple with different types of optical excitations such as Mie resonances [41], Fabry-Pérot (FP) cavity modes [42,43], and QBIC modes [44,45]. An enhanced coupling strength over 100 meV has been realized.

In addition to the BIC mode, which enables strong enhancement in the near field, an FP nanocavity is also capable of achieving field enhancement by confining external excitation light to an ultrasmall volume through multiple reflections [46–50]. Moreover, different orders of the FP nanocavity mode can be easily excited by adjusting the thickness of the microcavity, which provides convenient and flexible control of the interaction between the FP nanocavity mode and the optical resonators. Benefiting from these properties, strong coupling between the FP nanocavity mode and a plasmonic resonator has been reported [49,51,52]. Shegai *et al.* have experimentally demonstrated the collective strong light-matter coupling in cavity-assisted plasmon-X systems at room temperature by embedding gold nanoarrays and a WS_2 monolayer into a nanocavity [51]. So far, the cavity-assisted boosting of X-BIC self-hybridization in a strong-coupling regime has not been reported. Introducing an optical cavity to X-BIC coupling system is expected to take full advantage of the flexible tunability, large field enhancement, and low radiation loss properties of both resonant modes, which would greatly facilitate the enhancement of the coupling strength of the self-hybridized system.

In this paper, we report collective strong cavity-QBIC-X coupling at room temperature by embedding a 2D metasurface composed of bulk WS_2 into a microcavity. We demonstrate that the self-hybridized BIC-X coupling strength in this 2D metasurface can be dramatically enhanced with the assistance of an FP cavity. The optical property of the three-mode coupled system was obtained by full wave simulations, demonstrating a giant Rabi splitting up to 240 meV at ambient temperature, which is twice as high as the QBIC-X self-hybridization in the 2D metasurface system. A coupled oscillator model containing a 3×3 Hamiltonian matrix combined with a near-field analysis was utilized to reveal

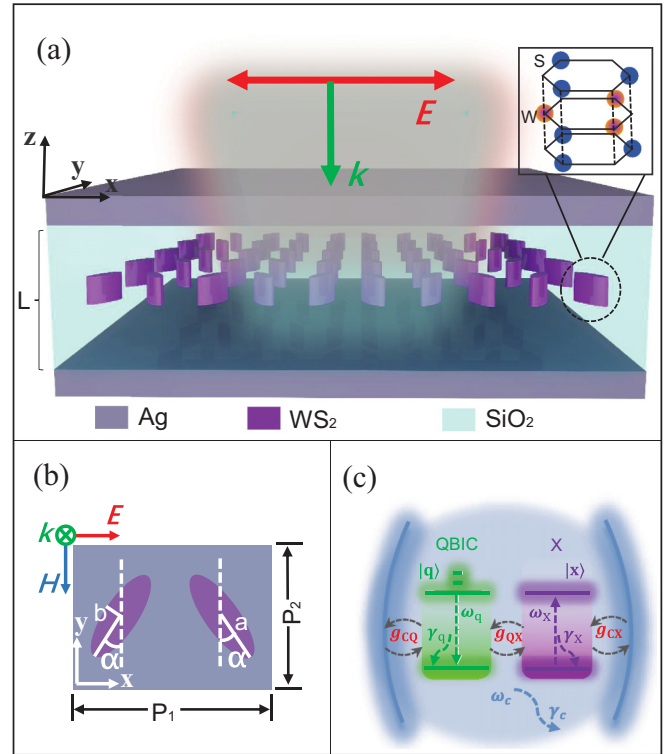


FIG. 1. (a) Three schematic diagrams of the coupling system: An elliptical bulk WS_2 array embedded in an FP cavity. The thickness of the silver film is 20 nm. (b) Parametric layout in an x - y plane: semiminor axis $b = 75$ nm, ellipse semimajor axis $a = 150$ nm. Periods P_1 and P_2 are $P_1 = 520$ nm and $P_2 = 440$ nm, respectively. The center spacing between elliptical bulk WS_2 is 260 nm, as well as the thickness of bulk WS_2 is 25 nm. The tilt angle α is fixed at 30° . (c) Schematic diagram of the oscillator model of the coupling system.

the underlying mechanism of the greatly enlarged coupling strength. Importantly, we also demonstrated the influence of the excitonic oscillator strength of the bulk TMD material on the coupling strength of the hybrid system. This provides a powerful approach for manipulating the self-hybridization process. We believe that the cavity-based configuration proposed in this paper can serve as a universal recipe for achieving strong light-matter interactions and is promising to provide different ideas for the design of ultracompact optical quantum devices.

II. RESULTS AND DISCUSSION

A. Strong-coupling system

The hybrid system, as shown in Fig. 1(a), consists of a 25-nm-thick 2D elliptical bulk WS_2 metasurface embedded in a silver FP microcavity. The schematic diagram of the cells in the x - y plane is shown in Fig. 1(b) with a detailed parameter layout. Numerical simulations based on the finite difference time domain (FDTD) were performed to investigate the coupling process of multiple photonic quasiparticles in this hybrid system. During the simulation a beam of planar light polarized along the x direction is incident perpendicular to the hybridized system, as shown in Fig. 1(b). Periodic boundary conditions are set in the x and y directions, and perfectly

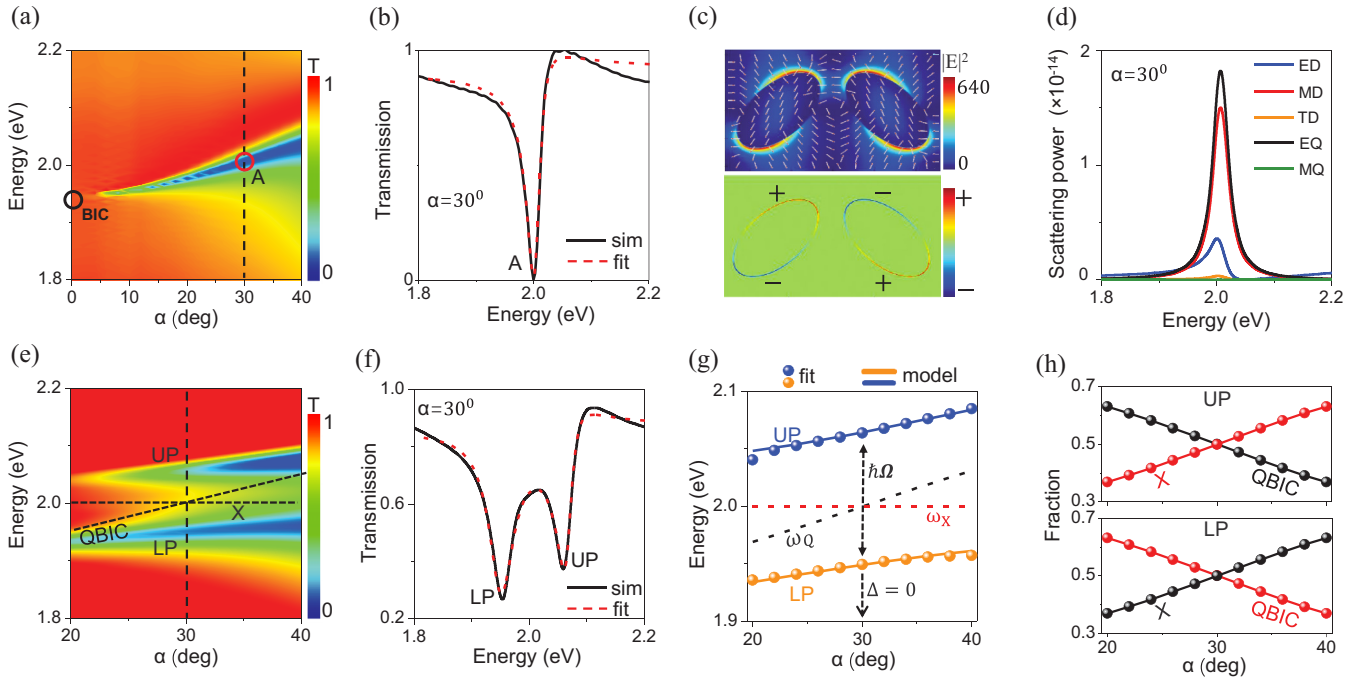


FIG. 2. (a) Transmission color map with different asymmetric parameters α ranging from 0° to 40° . (b) Simulating (solid black line) and fitting (dashed red line) the EQ-dominant resonance curve at $\alpha = 30^\circ$. (c) Enhanced distribution of electric field (top) and charge (bottom) distribution at $\alpha = 30^\circ$. (d) Calculated multipole decompositions of the unit cell exhibited in a scattering power plot. ED, MD, TD, EQ, and MQ represent the electric dipole moment, the magnetic dipole moment, the toroidal dipole moment, the electric quadrupole moment, and the magnetic quadrupole moment, respectively. (e) The transmission spectra of the QBIC-X system as a function of asymmetric parameter α (in color scale). (f) Simulating (solid black line) and fitting (dashed red line) the transmission curve of the hybrid system at zero detuning, i.e., $\alpha = 30^\circ$. (g) The dispersion curves of the strong QBIC-X coupling system obtained by the model (solid lines) and fitting the simulated spectra (sphere). The black and red dashed lines represent the uncoupled QBIC resonance and X, respectively. (h) The QBIC and X fractions in UP and LP.

matched layer (PML) conditions are used in the z direction. We set the mesh covering the whole simulation region to 1 nm to ensure the accuracy of the simulation results. The relative permittivity of Ag is determined by the CRC model (CRC Handbook of Chemistry & Physics). An isotropic permittivity is assumed for WS_2 . The dielectric function of the bulk WS_2 can be described by the classical Lorentzian oscillator as [43]

$$\epsilon(E) = \epsilon_B + \frac{f\omega_X^2}{\omega_X^2 - \omega^2 - i\omega\gamma_X}, \quad (1)$$

where $\epsilon_B = 20$ is the background permittivity induced by higher-energy transitions. $\hbar\omega_X = 2$ eV, $f = 0.2$, and $\hbar\gamma_X = 50$ meV represent the transition energy, the oscillator strength, and full linewidth of the excitonic mode, respectively. The permittivities of Ag and WS_2 exhibit a non-negligible imaginary part at frequencies, especially at 2 eV [Ag: real (-17), imaginary (2.2); WS_2 : real (20), imaginary (8)]. In addition, the refractive index of SiO_2 is set to $n = 1.45$ in the calculation.

The schematic diagram of the complete coupling process of the hybrid system is plotted in Fig. 1(c). In this three-mode system, the individual mode manifests as the FP cavity resonant energy $\hbar\omega_c$ with decay rate $\hbar\gamma_c$, the QBIC resonant energy $\hbar\omega_B$ with decay rate $\hbar\gamma_B$, and the excitonic quantum emitter (a two-level system) with transition energy $\hbar\omega_X$ and decay rate $\hbar\gamma_X$, respectively. The mutual QBIC-X, QBIC-cavity, and X-cavity coupling strengths are denoted by g_{QX} , g_{CQ} , and g_{CX} , respectively. The coupling eventually leads to

the formation of three eigenstates, namely the upper polariton (UP), the middle polariton (MP), and lower polariton (LP), which can be noticed in the spectrum in the form of a Rabi splitting. We can modulate the optical spectral peaks to obtain the anticrossing phenomenon of the eigenvalues, which is a typical feature of strong coupling.

B. BIC property in a bare 2D bulk WS_2 metasurface

We first explore the optical properties of the bare 2D metasurface constructed from background index-only material in the absence of an FP cavity by setting the oscillator strength f to 0. The symmetry of the metasurface in the x - y plane is broken by introducing the asymmetry parameter α [as shown in Fig. 1(b)] to achieve the symmetry-protected BIC to QBIC transition because of the spatial symmetry incompatibility between the bound state and the continuum. The simulated transmission spectrum with varying tilting angle α from 0° to 40° is shown in Fig. 2(a). The transmission spectra show that the symmetry-protected BIC mode with an infinite Q factor is excited at 1.94 eV, as marked by the black circle. The BIC is subsequently transformed into the QBIC mode with a finite Q factor by breaking the symmetry in the x - y plane (i.e., $\alpha \neq 0^\circ$).

To study the optical properties of the QBIC mode supported by the 2D metasurface, we extracted the transmission spectrum at $\alpha = 30^\circ$, which exhibits a sharp Fano resonance,

as shown in Fig. 2(b). The full width at half maximum (FWHM) of the QBIC mode, i.e., $\Gamma_Q = 2\gamma_Q$, can be obtained by fitting the spectrum to a Fano-type line-shape function $T(\omega) = |t(\omega)|^2$ with [18,53]

$$t(\omega) = a_b + \sum_{j=1}^N \frac{b_j \gamma_j e^{i\phi_j}}{\omega - \omega_j + i\gamma_j}. \quad (2)$$

Here, a_b , ϕ_j , and b_j are the background amplitude, phase, and amplitude of the transmission spectrum. The perfect agreement between the fitted curve [red dashed line in Fig. 2(b)] and the simulation result enables us to determine the resonant energy and damping rate of the QBIC mode to be $\hbar\omega_Q = 2$ eV and $\hbar\Gamma_Q = 2\hbar\gamma_Q = 28.6$ meV, respectively. This coupling system can also be directly calculated for coupling coefficients, frequencies, etc. [54].

We further studied the multipole characteristics of the QBIC model by combining the near-field analysis and the multipole expansion method. More information about the multipole expansion can be found in our previous work [24,33]. Figure 2(c) gives the electric field (top) distribution and charge (bottom) distribution of the A peak. Apparently, the electric field is mainly confined at the edge of the ellipse, indicating the formation of a magnetic dipole moment (MD) along the z direction and an electric quadrupole moment (EQ) in the x - y plane, respectively. Importantly, the electric field at the A-peak resonance is greatly enhanced by a factor of 640. Such a huge field enhancement plays a key role in the three-mode strong coupling, which will be discussed in detail in a later section. The domination of MD and EQ components in the QBIC mode can be further confirmed by the multipole expansion [55,56]. The scattering power plotted in Fig. 2(d) shows that the A peak is indeed dominated by MD and EQ multipoles simultaneously. Note that the scattering power of each multipole moment in our simulations is the sum of the cell along the x , y , and z directions. Indeed, a near-field analysis proves that the far-field radiation of both MD and EQ is distributed mainly in the x - y plane. In other words, the scattering power of MD and EQ multipoles in Fig. 2(d) is mainly contributed from the in-plane components.

C. Self-hybridized exciton polaritons in bulk WS₂

To realize self-hybridized exciton polaritons in bulk WS₂, we set the oscillator intensity f_0 to 0.2. The simulated transmission spectra (in color scale) as a function of tilting angle α are shown in Fig. 2(e). An anticrossing behavior is clearly visible in the spectra, indicating the strong coherent interaction of QBIC-X and the formation of hybrid UP and LP. To clarify the coupling effect of QBIC-X, we extracted the transmission spectrum at the anticrossing point ($\alpha = 30^\circ$), as shown in Fig. 2(f), where the two peaks corresponding to UP and LP can be clearly observed. The difference in transmission between the coupling system [Fig. 2(f)] and the QBIC mode [Fig. 2(b)] is caused by the imaginary part of the bulk WS₂ and the strong coupling. The former enhances the absorption and the latter is a phase difference between the two modes. Similarly, the simulated spectrum was fitted using Eq. (2) and

thus the energy difference between UP and LP, i.e., the Rabi splitting $\hbar\Omega_{\text{QX}}$, was determined as 122 meV.

To gain a deeper understanding of the interaction between the QBIC mode and X, we introduced the following widely used coupled oscillator model to quantitatively describe the coherent coupling process [57],

$$\hbar \begin{pmatrix} \omega_Q - i\gamma_Q & g_{\text{QX}} \\ g_{\text{QX}} & \omega - i\gamma_X \end{pmatrix} \begin{pmatrix} \alpha \\ \beta \end{pmatrix} = \hbar\omega_{\pm} \begin{pmatrix} \alpha \\ \beta \end{pmatrix}. \quad (3)$$

Here, $\hbar\omega_Q$ and $\hbar\Gamma_Q = 2\hbar\gamma_Q = 28.6$ meV are the resonant energy and linewidth of the uncoupled QBIC mode. $\hbar\omega_X$ and $\hbar\Gamma_X = 2\hbar\gamma_X = 50$ meV represent the transition energy and linewidth of the X in bulk WS₂. α and β are the components of the eigenvectors satisfying $|\alpha|^2 + |\beta|^2 = 1$. By diagonalizing Eq. (3), the dispersion of polariton modes corresponding to UP and LP, i.e., E_+ and E_- , can be calculated as

$$E_{\pm} = \hbar\omega_{\pm} = \frac{\hbar}{2} \left[(\omega_Q + \omega_X - i\gamma_X - i\gamma_Q) \pm \sqrt{4g_{\text{QX}}^2 + [\omega_Q - \omega_X - i(\gamma_X - \gamma_Q)]^2} \right]. \quad (4)$$

At zero detuning with $\omega_Q = \omega_X$, the Rabi splitting can be expressed as

$$g_{\text{QX}} = \frac{1}{2} \sqrt{\Omega_{\text{QX}}^2 + (\gamma_X - \gamma_Q)^2}. \quad (5)$$

To ensure that the QBIC-X system enters the strong-coupling range, two conditions must be satisfied, i.e., $g_{\text{QX}} > |\gamma_X - \gamma_Q|/2$ and $g_{\text{QX}} > \sqrt{(\gamma_X^2 + \gamma_Q^2)}/2$. The former is to confirm the presence of Rabi splitting, and the latter is to ensure that Rabi splitting can be observed experimentally.

We calculated the coupling strength g_{QX} between the QBIC mode and the X to be 61.234 meV by Eq. (5). Introducing the coupling strength $g_{\text{QX}} = 61.234$ meV into Eq. (6), we can notice that the dispersion of the hybrid states (solid blue line: UP; solid yellow line: LP) and the fitted results (blue sphere: UP; yellow sphere: LP) are in perfect agreement, as shown in Fig. 2(g). In addition, we find that the current case satisfies both of the previous cases, i.e., $\hbar g_{\text{QX}} > |\gamma_X - \gamma_Q|/2$ and $\hbar g_{\text{QX}} > \sqrt{(\gamma_X^2 + \gamma_Q^2)}/2$, demonstrating the formation of the exciton polarization state. The fractions of the QBIC mode and X mode in UP and LP are given in Fig. 2(h), indicating the presence of energy exchange processes.

Although we have demonstrated strong coupling between the QBIC modes and X supported by 2D bulk WS₂ metasurfaces simultaneously, the current coupling strength g_{QX} is limited. We next achieve a further enhancement of the coupling strength by introducing the FP cavity mode.

D. Three-mode cavity-QBIC-X hybrid system

We first set the tilting angle α and the oscillator strength f of the 2D metasurface to 0° and 0, respectively, and subsequently embedded it into the FP cavity formed by two silver layers separated by SiO₂. Figure 3(a) gives the transmission spectrum (in color scale) of the FP cavity as a function of the thickness L . We can note that the resonant energy of the FP cavity transforms from 2.08 to 1.93 meV by varying the thickness L from 80 to 112 nm, which would cross the zero detuning point of the strong QBIC-X coupling system.

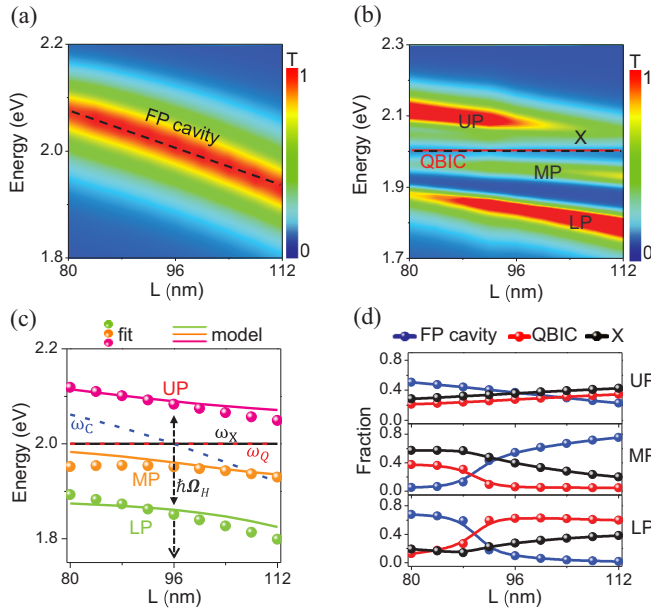


FIG. 3. (a) Transmission spectrum of a pure cavity with different thicknesses L ranging from 80 to 112 nm. The black dashed line represent the dispersion curve of the cavity mode. (b) Transmission color map of the hybrid system as a function of the thickness (L) of cavity. The red dashed line and black dashed line represent the QBIC mode and the X resonance peak, respectively, which are strictly at the same resonance position. (c) The dispersions curves of the hybrid states obtained by the model (solid lines) and fitting the simulated spectra (sphere). (d) The cavity, QBIC, and X fractions in UP, MP, and LP.

Subsequently, the tilting angle and oscillator strength of the 2D bulk WS_2 metasurface are restored to $\alpha = 30^\circ$ and $f = 0.3$ to turn on the QBIC mode and excitonic state. We can clearly note the formation of three hybrid states by sweeping the transmission spectra of the FP cavity-QBIC-X system as a function of the thickness of the FP cavity, i.e., UP, MP, and LP, as shown in Fig. 3(b). By fitting the transmission spectrum obtained from the simulation by Eq. (2), we have plotted the dispersion curves of the hybrid states (pink sphere: UP; yellow sphere: MP; green sphere: LP) formed by the coupling in Fig. 3(c). Similarly, to further investigate the Rabi splitting and coupling strength of the current coupled system, we construct the following 3×3 coupled resonant oscillator model [58,59],

$$\hbar \begin{pmatrix} \omega_Q - i\gamma_Q & g_{QX} & g_{CQ} \\ g_{QX} & \omega_X - i\gamma_X & g_{CX} \\ g_{CQ} & g_{CX} & \omega_C - i\gamma_C \end{pmatrix} \begin{pmatrix} V_1 \\ V_2 \\ V_3 \end{pmatrix} = \hbar\omega_H \begin{pmatrix} V_1 \\ V_2 \\ V_3 \end{pmatrix}. \quad (6)$$

Here, $\hbar g_{QX} = 90$ meV, $\hbar g_{CQ} = 65$ meV, and $\hbar g_{CX} = 61.234$ meV are the coupling strengths of the FP cavity-QBIC, FP cavity-X, and QBIC-X coupling systems, respectively. V_1 , V_2 , and V_3 are weighting coefficients, which satisfy $|V_1|^2 + |V_2|^2 + |V_3|^2 = 1$ as shown in Fig. 3(d). Here, we define the Rabi splitting of the three-coupled-oscillator model as the

energy difference between UP and LP, which is similar to that of the two-coupled-oscillator subsystem. When $L = 96$ nm we note that the resonance energies of the UP and LP states are 2.085 and 1.845 eV, respectively, which indicates that the Rabi splitting of the FP cavity-QBIC-X coupled system is $\hbar\Omega_H = 240$ meV. It is apparent that for the current three-mode oscillator system the Rabi splitting is much greater than that of any two-mode oscillator system (FP cavity-QBIC system: 180 meV; FP cavity-X system: 130 meV; QBIC-X system: 122 meV).

For the current FP cavity-QBIC-X coupling system, the criteria for determining the strong coupling can be expressed as

$$\Omega_H > W_{UP}\Gamma_{UP} + W_{MP}\Gamma_{MP} + W_{LP}\Gamma_{LP}, \quad (7)$$

where W_{UP} , W_{MP} , and W_{LP} are the weighting coefficients of UP, MP, and LP states in the FP cavity-QBIC-X heterostructure. Γ_{UP} , Γ_{MP} , and Γ_{LP} represent the linewidths of the corresponding subsystem, respectively. Therefore, the weight contribution of its corresponding three branches can be calculated as

$$\begin{aligned} W_{UP} &= \Gamma_{UP}/(\Gamma_{UP} + \Gamma_{MP} + \Gamma_{LP}), \\ W_{MP} &= \Gamma_{MP}/(\Gamma_{UP} + \Gamma_{MP} + \Gamma_{LP}), \\ W_{LP} &= \Gamma_{LP}/(\Gamma_{UP} + \Gamma_{MP} + \Gamma_{LP}). \end{aligned} \quad (8)$$

Subsequently, the linewidths of the three branches of the hybrid state can be obtained from the FP cavity mode, QBIC mode, and X mode fractions as shown in Fig. 3(d),

$$\begin{aligned} \Gamma_{UP} &= 36.8\%\Gamma_C + 27.6\%\Gamma_Q + 35.6\%\Gamma_X, \\ \Gamma_{MP} &= 54.4\%\Gamma_C + 6.1\%\Gamma_Q + 39.5\%\Gamma_X, \\ \Gamma_{LP} &= 9.8\%\Gamma_C + 62.5\%\Gamma_Q + 27.7\%\Gamma_X. \end{aligned} \quad (9)$$

Therefore, by substituting Eqs. (8) and (9) into Eq. (7), we can obtain the criterion for the strong coupling of the FP cavity-QBIC-X heterostructure as follows:

$$\Omega_H > 32.4\%\Gamma_C + 33.5\%\Gamma_Q + 34.1\%\Gamma_X. \quad (10)$$

For the current case, $\hbar\Omega_H = 240$ meV, $\hbar\Gamma_C = 114.4$ meV, $\hbar\Gamma_Q = 28.6$ meV, and $\hbar\Gamma_X = 50$ meV. It is obvious that the criterion for strong coupling is satisfied in the coupling system. More importantly, the Rabi splitting value is almost twice that of the strong QBIC-X coupling system, which indicates that the strong coupling between the QBIC mode and X is greatly enhanced by the introduction of the FP cavity.

To gain insight into the physical mechanism behind the current enhanced coherent coupling strength, we quantified the near-field characteristics of the FP cavity mode and the QBIC mode. Figures 4(a)–4(c) illustrate the near-field distribution of the electric components of the FP cavity mode in the x - z plane in the x , y , and z directions for the thickness of the microcavity $L = 96$ nm, tilting angle $\alpha = 0^\circ$ of the 2D metasurface, and the oscillator strength $f = 0$, respectively. It can be noted that the electric field strengths of the x and z components are enhanced by a factor of 174 and 122, respectively, compared to the amplitude of the incident electric field, which is a considerable field confinement capability. Similarly, Figs. 4(d)–4(f) demonstrate the near-field distributions of the electric components in the x - y plane in the x , y , and z directions for the QBIC

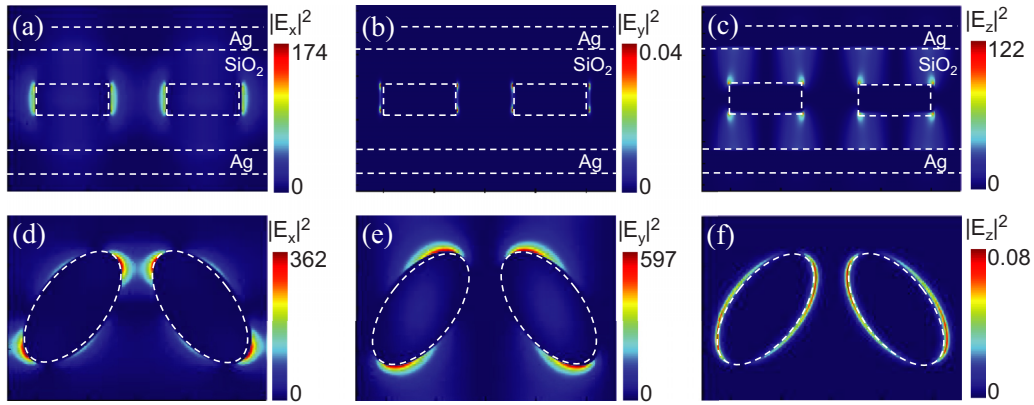


FIG. 4. (a)–(c) Electric field distribution of the FP cavity resonance mode in the x - z plane in the x , y , and z directions. (d), (e) Electric field distribution of QBIC resonance mode in the x - y plane in the x , y , and z directions.

mode at a tilting angle $\alpha = 30^\circ$ and the oscillator strength $f = 0$ for the 2D metasurface, respectively. We can observe that the x - and z -component electric fields provide us with up to 362- and 597-fold enhancements under the excitation of the incident electric field, respectively.

Compared with the case of strong coupling of single quantum emitters, the total coupling strength g is the sum of the coupling strengths $g_i(r)$ of the individual excitons involved in the coupling, i.e., $g = \sum g_i(r) = \mu \cdot \mathbf{E}_i(\mathbf{r})$, where μ is the dipole moment of the quantum emitter and $\mathbf{E}_i(\mathbf{r})$ represents the in-plane component of the electric field at position r_i [62]. For the current case, both intralayer excitons and interlayer excitons are present within the three-dimensional (3D) bulk WS_2 , which is completely distinct from the monolayer WS_2 with only in-plane excitons. The configuration of the coupling system, such as the thickness of the microcavity, the selection of materials, and the model size, is optimized so that the QBIC mode in the x - y plane and the FP cavity mode in the x - z plane displays a significant enhancement of the electric field. These properties greatly facilitate the coupling of the intra- and interlayer excitons of the bulk WS_2 to the local electric field in the x - y and x - z planes, respectively, and ultimately contribute to the current Rabi splitting of up to 240 meV.

In addition, we have done something similar to the previous work: We artificially modulated the oscillator strength of X of the bulk WS_2 to study its effect on the current hybrid system. Figures 5(a) and 5(b) give the transmission spectra of the hybrid system as a function of the FP cavity thickness L for oscillator strengths $f = 0.9$ and $f = 1.5$, respectively. It can be clearly noticed that the anticrossing behavior caused by the strong coupling is more pronounced with an increase of the oscillator strength f . We also calculated the transmission spectrum of the hybrid system at zero detuning as a function of the oscillator strength f in order to explicitly observe the trend of the hybrid state with the oscillator strength f , as shown in Fig. 5(c). The UP gradually shifts blue while the MP and LP slowly shift red with increasing oscillator strength f , which widens the difference between the UP and LP. The differences of UP and LP, i.e., Rabi splitting, are plotted in Fig. 5(d) for the QBIC-X system (black curve) and the FP cavity-QBIC-X system (red curve), respectively, indicating

that the FP cavity greatly enhances the coupling strength for the QBIC-X hybrid system at an arbitrary oscillator strength. In particular, the Rabi splitting of the FP cavity-QBIC-X system is $\Omega_H = 464$ meV when the oscillator strength f is increased to 1.5, which, to the best of our knowledge, is the maximum value reported so far for a QBIC-X system constructed based on TMDs. To compare our results with other QBIC-X systems, Table I lists the Rabi splitting obtained by other structural layouts of the QBIC-X system. It can be observed that the great enhancement of the Rabi splitting is achieved by the introduction of the FP cavity leading to the

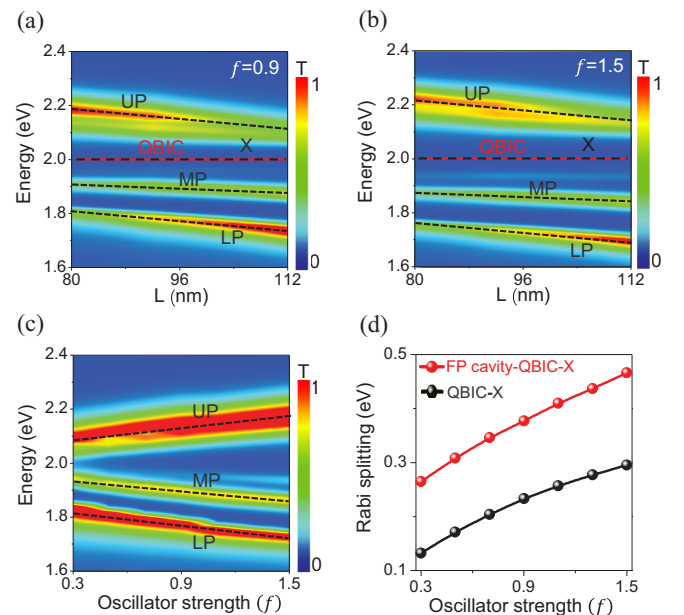


FIG. 5. The transmission spectrum (in color scale) of the hybrid system with different oscillator strengths (a) $f = 0.9$ and (b) $f = 1.5$. (c) The transmission spectrum of the coupling system at zero detuning as a function of the oscillator strength of X ranging from 0.3 to 1.5. (d) The trend of Rabi splitting with oscillator strength from 0.3 to 1.5 for the two coupled systems. The black curve and the red curve represent the QBIC-X and cavity-QBIC-X hybrid systems, respectively.

TABLE I. Comparison of strong coupling between different QBIC modes and X in TMDs.

| Structure | Mode | Rabi splitting (meV) | Ref. No. |
|-------------------------------------------------------------------------------------------------------------------------------------------|------------------|----------------------|-----------|
| Monolayer WSe ₂ on Ta ₂ O ₅ grating | QBIC-X | 5.7 | [37] |
| Monolayer MoSe ₂ on Ta ₂ O ₅ grating | QBIC-X | 27 | [31] |
| Monolayer WS ₂ on SiN grating | QBIC-X | 28.4 | [38] |
| Monolayer WS ₂ on TiO ₂ metasurface | MD QBIC-X | 33.83 | [39] |
| Monolayer WS ₂ on Si metasurface | MD QBIC-X | 34 | [33] |
| Monolayer WSe ₂ /WS ₂ /MoSe ₂ /MoS ₂ in Si ₃ N ₄ grating/metasurface | MD/TD QBIC-X | 38/65/40/60 | [40] |
| Monolayer WS ₂ with dielectric metasurface | QBIC cavity-X | 64.1/63.8/58 | [60] |
| Monolayer WS ₂ on TiO ₂ metasurface | MD QBIC-X | 29.33 | [61] |
| Grating formed by bulk WS ₂ | QBIC-X | 120/45 | [44] |
| Grating formed by bulk WS ₂ | QBIC-X | 162 | [45] |
| Bulk WS ₂ embedded in FP cavity | FP cavity-QBIC-X | 464 | This work |

expansion of the number of photonic quasiparticles from 2 to 3, which provides a good idea for us to subsequently design more attractive platforms to explore light-matter interactions in strong coupling.

III. CONCLUSIONS

To conclude, combining numerical simulations with a theoretical analysis, we have successfully demonstrated a collective FP cavity-QBIC-X strong coupling by constructing a microcavity containing a bulk WS₂ metasurface configuration. We confirm the Rabi splitting of the coupled system up to 240 meV with the assistance of a three-oscillator model, which is the maximum value reported for strong QBIC-X coupled systems constructed based on TMDs so far. This is due to the strong field enhancement triggered by the excellent spatial overlap of the FP cavity mode and the QBIC mode, which

contributes to the full coupling of the intra- and interlayer excitons in the bulk WS₂ and local fields. Importantly, the Rabi splitting of the current coupling system can be further enhanced by adjusting the oscillator strength to 464 meV. By expanding the number of photonic quasiparticles from two to three, this coupling system promises to be a great platform for studying strong light-matter interactions and offers potential applications for realizing ultrafast optical switches and different quantum devices.

ACKNOWLEDGMENTS

This work was supported by the National Natural Science Foundation of China (Grants No. 11974254 and No. 11974253), Science Specialty Program of Sichuan University (Grant No. 2020SCUNL210), and the Innovation Program of Sichuan University (Grant No. 2018SCUH0074).

-
- [1] J. Kasprzak, M. Richard, S. Kundermann, A. Baas, P. Jeambrun, J. M. J. Keeling, F. M. Marchetti, M. H. Szymanska, R. Andre, J. L. Staehli, V. Savona, P. B. Littlewood, B. Deveaud, and L. S. Dang, *Nature (London)* **443**, 409 (2006).
- [2] K. Hennessy, A. Badolato, M. Winger, D. Gerace, M. Atature, S. Gulde, S. Falt, E. L. Hu, and A. Imamoglu, *Nature (London)* **445**, 896 (2007).
- [3] G. Khitrova, H. M. Gibbs, M. Kira, S. W. Koch, and A. Scherer, *Nat. Phys.* **2**, 81 (2006).
- [4] P. Torma and W. L. Barnes, *Rep. Prog. Phys.* **78**, 013901 (2015).
- [5] A. Elbanna, K. Chaykun, Y. Lekina, Y. Liu, B. Febriansyah, S. Li, J. Pan, Z. X. Shen, and J. Teng, *Opto-Electron. Sci.* **1**, 220006 (2022).
- [6] L. J. Huang, A. Krasnok, A. Alu, Y. L. Yu, D. Neshev, and A. E. Miroshnichenko, *Rep. Prog. Phys.* **85**, 046401 (2022).
- [7] H. Deng, H. Haug, and Y. Yamamoto, *Rev. Mod. Phys.* **82**, 1489 (2010).
- [8] A. Amo, J. Lefrere, S. Pigeon, C. Adrados, C. Ciuti, I. Carusotto, R. Houdre, E. Giacobino, and A. Bramati, *Nat. Phys.* **5**, 805 (2009).
- [9] M. D. Fraser, S. Hofling, and Y. Yamamoto, *Nat. Mater.* **15**, 1049 (2016).
- [10] L. Y. Sun, C. Y. Wang, A. Krasnok, J. Choi, J. W. Shi, J. S. Gomez-Diaz, A. Zepeda, S. Gwo, C. K. Shih, A. Alu, and X. Q. Li, *Nat. Photonics* **13**, 180 (2019).
- [11] D. G. Baranov, M. Wersall, J. Cuadra, T. J. Antosiewicz, and T. Shegai, *ACS Photonics* **5**, 24 (2018).
- [12] S. Y. Hou, L. Y. M. Tobing, X. L. Wang, Z. W. Xie, J. H. Yu, J. Zhou, D. H. Zhang, C. Dang, P. Coquet, B. K. Tay, M. D. Birowosuto, E. H. T. Teo, and H. Wang, *Adv. Opt. Mater.* **7**, 1900857 (2019).
- [13] X. B. Han, K. Wang, X. Y. Xing, M. Y. Wang, and P. X. Lu, *ACS Photonics* **5**, 3970 (2018).
- [14] M.-E. Kleemann, R. Chikkaraddy, E. M. Alexeev, D. Kos, C. Carnegie, W. Deacon, A. C. de Pury, C. Grosse, B. de Nijs, J. Mertens, A. I. Tartakovskii, and J. J. Baumberg, *Nat. Commun.* **8**, 1296 (2017).
- [15] J. B. Lassiter, F. McGuire, J. J. Mock, C. Ciraci, R. T. Hill, B. J. Wiley, A. Chilkoti, and D. R. Smith, *Nano Lett.* **13**, 5866 (2013).

- [16] J. Wen, H. Wang, W. Wang, Z. Deng, C. Zhuang, Y. Zhang, F. Liu, J. She, J. Chen, H. Chen, S. Deng, and N. Xu, *Nano Lett.* **17**, 4689 (2017).
- [17] W. Zhang, J.-B. You, J. Liu, X. Xiong, Z. Li, C. E. Png, L. Wu, C. W. Qiu, and Z. K. Zhou, *Nano Lett.* **21**, 8979 (2021).
- [18] P. Xie, Z. Liang, Z. Li, W. Wang, W. Wang, T. Xu, X. Kuang, L. Qing, D. Li, and J. Yi, *Phys. Rev. B* **101**, 045403 (2020).
- [19] P. Xie, D. Li, Y. Chen, P. Chang, H. Zhang, J. Yi, and W. Wang, *Phys. Rev. B* **102**, 115430 (2020).
- [20] N. T. Fofang, T. H. Park, O. Neumann, N. A. Mirin, P. Nordlander, and N. J. Halas, *Nano Lett.* **8**, 3481 (2008).
- [21] J. W. Sun, H. T. Hu, D. Zheng, D. X. Zhang, Q. Deng, S. P. Zhang, and H. X. Xu, *ACS Nano* **12**, 10393 (2018).
- [22] G. V. Naik, V. M. Shalaev, and A. Boltasseva, *Adv. Mater.* **25**, 3264 (2013).
- [23] J. B. Khurgin, *Nat. Nanotechnol.* **10**, 2 (2015).
- [24] S. Y. Shen, Y. Y. Wu, Y. H. Li, P. Xie, Q. Ding, X. Y. Kuang, W. X. Wang, and W. Wang, *Phys. Rev. B* **105**, 155403 (2022).
- [25] H. Wang, J. X. Wen, W. L. Wang, N. S. Xu, P. Liu, J. H. Yang, H. J. Chen, and S. Z. Deng, *ACS Nano* **13**, 1739 (2019).
- [26] S. Lepeshov, M. S. Wang, A. Krasnok, O. Kotov, T. Y. Zhang, H. Liu, T. Z. Jiang, B. Korgel, M. Terrones, Y. B. Zheng, and A. Alu, *ACS Appl. Mater. Interfaces* **10**, 16690 (2018).
- [27] M. L. Brongersma, Y. Cui, and S. H. Fan, *Nat. Mater.* **13**, 451 (2014).
- [28] R. M. Bakker, D. Permyakov, Y. F. Yu, D. Markovich, R. Paniagua-Dominguez, L. Gonzaga, A. Samusev, Y. Kivshar, B. Luk'yanchuk, and A. I. Kuznetsov, *Nano Lett.* **15**, 2137 (2015).
- [29] A. I. Kuznetsov, A. E. Miroshnichenko, M. L. Brongersma, Y. S. Kivshar, and B. Luk'yanchuk, *Science* **354**, 2472 (2016).
- [30] Y. Yang, O. D. Miller, T. Christensen, J. D. Joannopoulos, and M. Soljacic, *Nano Lett.* **17**, 3238 (2017).
- [31] V. Kravtsov, E. Khestanova, F. A. Benimetskiy, T. Ivanova, A. K. Samusev, I. S. Sinev, D. Pidgayko, A. M. Mozharov, I. S. Mukhin, M. S. Lozhkin, Y. V. Kapitonov, A. S. Brichtkin, V. D. Kulakovskii, I. A. Shelykh, A. I. Tartakovskii, P. M. Walker, M. S. Skolnick, D. N. Krizhanovskii, and I. V. Iorsh, *Light: Sci. Appl.* **9**, 56 (2020).
- [32] N. Bernhardt, K. Koshelev, S. J. U. White, K. W. C. Meng, J. E. Froch, S. Kim, T. Toan Trong, D.-Y. Choi, Y. Kivshar, and A. S. Solntsev, *Nano Lett.* **20**, 5309 (2020).
- [33] P. Xie, Z. C. Liang, T. T. Jia, D. M. Li, Y. X. Chen, P. J. Chang, H. Zhang, and W. Wang, *Phys. Rev. B* **104**, 125446 (2021).
- [34] K. Koshelev, A. Bogdanov, and Y. Kivshar, *Sci. Bull.* **64**, 836 (2019).
- [35] C. Fang, Q. Yang, Q. Yuan, X. Gan, J. Zhao, Y. Shao, Y. Liu, G. Han, and Y. Hao, *Opto-Electron. Adv.* **4**, 200030 (2021).
- [36] P. L. Hong, L. Xu, and M. Rahmani, *Opto-Electron. Adv.* **5**, 200097 (2022).
- [37] K. L. Koshelev, S. K. Sychev, Z. F. Sadrieva, A. A. Bogdanov, and I. V. Iorsh, *Phys. Rev. B* **98**, 161113(R) (2018).
- [38] S. Cao, H. G. Dong, J. L. He, E. Forsberg, Y. Jin, and S. L. He, *J. Phys. Chem. Lett.* **11**, 4631 (2020).
- [39] M. B. Qin, S. Y. Xiao, W. X. Liu, M. Y. Ouyang, T. B. Yu, T. B. A. Wang, and Q. H. Liao, *Opt. Express* **29**, 18026 (2021).
- [40] I. A. M. Al-Ani, K. As'Ham, L. J. Huang, A. E. Miroshnichenko, and H. T. Hattori, *Laser Photonics Rev.* **15**, 2100240 (2021).
- [41] R. Verre, D. G. Baranov, B. Munkhbat, J. Cuadra, M. Kall, and T. Shegai, *Nat. Nanotechnol.* **14**, 679 (2019).
- [42] Q. Wang, L. X. Sun, B. Zhang, C. Q. Chen, X. C. Shen, and W. Lu, *Opt. Express* **24**, 7151 (2016).
- [43] B. Munkhbat, D. G. Baranov, M. Stuhrenberg, M. Wersall, A. Bisht, and T. Shegai, *ACS Photonics* **6**, 139 (2019).
- [44] X. Y. Zong, L. X. Li, and Y. F. Liu, *Opt. Lett.* **46**, 6095 (2021).
- [45] J. Wu and Y. M. Qing, *Phys. Chem. Chem. Phys.* **24**, 23382 (2022).
- [46] R. Ameling and H. Giessen, *Nano Lett.* **10**, 4394 (2010).
- [47] X. T. Yu, Y. F. Yuan, J. H. Xu, K. T. Yong, J. L. Qu, and J. Song, *Laser Photonics Rev.* **13**, 1800219 (2019).
- [48] Z. Jiang, Y. Liu, and L. Wang, *Opto-Electron. Sci.* **1**, 210004 (2022).
- [49] B. W. Li, S. Zu, Z. P. Zhang, L. H. Zheng, Q. Jiang, B. W. Du, Y. Luo, Y. J. Gong, Y. F. Zhang, F. Lin, B. Shen, X. Zhu, P. M. Ajayan, and Z. Y. Fang, *Opto-Electron. Adv.* **2**, 190008 (2019).
- [50] A. Q. Hu, S. Liu, J. Y. Zhao, T. Wen, W. D. Zhang, Q. H. Gong, Y. Q. Meng, Y. Ye, and G. W. Lu, *Opto-Electron. Adv.* **3**, 190017 (2020).
- [51] A. Bisht, J. Cuadra, M. Wersall, A. Canales, T. J. Antosiewicz, and T. Shegai, *Nano Lett.* **19**, 189 (2019).
- [52] P. Peng, Y. C. Liu, D. Xu, Q. T. Cao, G. Lu, Q. H. Gong, and Y. F. Xiao, *Phys. Rev. Lett.* **119**, 233901 (2017).
- [53] Z. C. Liang, L. Y. Qing, Z. J. Li, X. T. Nguyen, T. Xu, A. De Sio, H. Zhang, C. Lienau, and W. Wang, *Phys. Rev. B* **102**, 035422 (2020).
- [54] O. Tsilipakos, T. Christopoulos, and E. E. Kriezis, *J. Lightwave Technol.* **34**, 1333 (2016).
- [55] C. Zhou, S. Li, Y. Wang, and M. Zhan, *Phys. Rev. B* **100**, 195306 (2019).
- [56] S. Li, C. Zhou, T. Liu, and S. Xiao, *Phys. Rev. A* **100**, 063803 (2019).
- [57] W. Wang, P. Vasa, R. Pomraenke, R. Vogelgesang, A. De Sio, E. Sommer, M. Maiuri, C. Manzoni, G. Cerullo, and C. Lienau, *ACS Nano* **8**, 1056 (2014).
- [58] K. As'ham, I. Al-Ani, L. J. Huang, A. E. Miroshnichenko, and H. T. Hattori, *ACS Photonics* **8**, 489 (2021).
- [59] F. Deng, H. X. Huang, J. D. Chen, S. M. Liu, H. J. Pang, X. B. He, and S. Lan, *Nano Lett.* **22**, 220 (2022).
- [60] X. Zhang and A. L. Bradley, *Phys. Rev. B* **105**, 165424 (2022).
- [61] M. B. Qin, J. Y. Duan, S. Y. Xiao, W. X. Liu, T. B. Yu, T. B. Wang, and Q. H. Liao, *Phys. Rev. B* **105**, 195425 (2022).
- [62] P. Xie, Y. Y. Wu, Y. H. Li, P. J. Chang, H. Zhang, and W. Wang, *J. Opt.* **24**, 093001 (2022).